Statistical Analysis of Experimental Factors for Synthesis of Copper Oxide and Tin Oxide for Antibacterial Applications

Mohammad Rezayat [1]*, Mojtaba Karamimoghadam[2], Morteza Saghafi Yazdi[3], Mahmoud Moradi[4] and Mahdi Bodaghi[5]*

[1] Center for Structural Integrity, Micromechanics, and Reliability of Materials (CIEFMA)-Department of Materials Science and Engineering, Universitat Politècnica de Catalunya-BarcelonaTECH, 08019 Barcelona, Spain.

[2] Department of Mechanics, Mathematics and Management, Polytechnic University of Bari, Via Orabona 4, 70125 Bari, Italy.

[3] Department of Materials Science and Engineering, Faculty of Engineering, Imam Khomeini International University, PO, 34149-16818, Qazvin, Iran.

[4] Faculty of Arts, Science and Technology, University of Northampton, Northampton, NN1 5PH, UK.

[5] Department of Engineering, School of Science and Technology, Nottingham Trent University, Nottingham NG11 8NS, UK.

* Corresponding authors: mohammad.rezayat@upc.edu; mahdi.bodaghi@ntu.ac.uk

Abstract

This research explores the impact of Cu Composition, Heating Temperature, and Milling Time on the production of copper-tin alloy nanoparticles. By employing Design of Experiments techniques, the study systematically evaluates these input variables and their effects on Particle Size, Optical Density, and Number of Colonies. The identification of new Cu_3Sn phases in the nanoparticle structure contributes to the novelty of this research. The findings highlight the potential for optimizing copper-tin alloy nanoparticle synthesis and enhancing their antibacterial properties. Mechanical alloying is found to produce nanoparticles up to 15 nm in size. Increasing the percentage of copper leads to improved antibacterial properties. This work provides insights into the synthesis process of copper-tin mechanical alloying and their potential for antibacterial applications.

Keywords: Copper-tin nanoparticles; Mechanical milling; Antibacterial applications; Statistical analysis; Response surface methodology

1. Introduction

Antibacterial copper and tin oxide nanoparticles have emerged as promising alternatives to traditional antibiotics due to their unique physicochemical properties and superior antibacterial activity [1,2]. These nanoparticles can effectively inhibit bacterial growth and prevent the spread of antibiotic-resistant bacterial strains [3–5]. However, synthesizing these nanoparticles requires careful optimization of experimental factors to achieve desirable properties. Copper oxide and tin oxide nanoparticles have gained attention for their antibacterial properties due to their unique surface chemistry and size-dependent reactivity [6,7]. Copper oxide nanoparticles exhibit strong antibacterial activity by inducing oxidative stress and damaging the bacterial cell wall and membrane [8]. Tin oxide nanoparticles, on the other hand, exhibit antibacterial activity by generating reactive oxygen species (ROS) and disrupting the bacterial membrane potential [9]. Therefore, the optimization of the synthesis of copper oxide and tin oxide nanoparticles with enhanced antibacterial activity is crucial for their potential application as antibacterial agents.

Recently, mechanical milling has emerged as an effective method for the synthesis of copper oxide and tin oxide nanoparticles due to its simplicity, scalability, and cost-effectiveness [10–13]. Mechanical milling involves the grinding of bulk materials in the presence of a reducing agent to produce nanoparticles. The synthesis of copper oxide and tin oxide nanoparticles by mechanical milling has been reported in several studies [14,15]. However, the optimization of the mechanical milling process for the synthesis of antibacterial copper oxide and tin oxide nanoparticles has not been extensively investigated. Statistical analysis techniques have been widely used to optimize nanoparticle synthesis processes in recent years. These techniques enable the systematic investigation of various factors that affect nanoparticle synthesis and provide a means to optimize experimental conditions for the desired properties. One commonly used statistical approach is the Design of Experiments (DOE)

methodology [16–18], which can efficiently screen multiple factors and their interactions to identify the most influential factors and optimize their levels.

Several studies have employed DOE methodology to optimize the synthesis of copper and tin oxide nanoparticles. Bahloul et al. [19] used a full factorial design to investigate the effects of various synthesis parameters on the size and morphology of copper oxide nanoparticles. Their study revealed that copper precursor concentration and reaction time significantly affect the size and morphology of the nanoparticles. Similarly, Dong et al. [20] utilized a response surface methodology to optimize the synthesis of tin oxide nanoparticles for enhanced photocatalytic activity. Moghaddam and Mirzaei have focused on the optimization of copper oxide and tin oxide nanoparticle synthesis using various methods, including sol-gel, hydrothermal, and microwave-assisted methods [21–24]. In addition, statistical approaches, such as response surface methodology (RSM) and Taguchi method, have been utilized to optimize the synthesis parameters for copper oxide and tin oxide nanoparticles [25,26].

The advancements in the field of nanochemistry and the synthesis of nanoparticles in diminishing dimensions was reviewed by Calvo [27] . The review highlights the importance of optimizing the synthesis conditions to obtain desired nanoparticle properties. In addition, Paulose et al. [28] optimized the synthesis of CuO nanoparticles using DOE methodology and investigated their catalytic activity for thermal decomposition of ammonium perchlorate. Their study revealed that the optimized synthesis conditions resulted in nanoparticles with higher catalytic activity. Zhu et al. [29] used a DOE approach to optimize the synthesis of palladium nanoparticles supported on carbon nanotubes for use as a catalyst in the hydrogenation of nitrobenzene. They found that the palladium loading and calcination temperature significantly affected the catalytic activity of the nanoparticles. Similarly, Alam et al. [30] used a DOE approach to optimize the synthesis of nickel nanoparticles supported on activated carbon for

the removal of organic pollutants from wastewater. They found that the reaction temperature and nickel loading significantly affected the removal efficiency of the nanoparticles. For instance, response surface methodology (RSM) has been employed to optimize the synthesis of titanium dioxide nanoparticles with enhanced photocatalytic activity [31]. The research study found that the reaction time, temperature, and precursor concentration significantly affected the photocatalytic activity of the nanoparticles. Optimizing the synthesis of silver nanoparticles using the response surface methodology (RSM) and investigates the effects of various synthesis parameters on the size and stability of the nanoparticles. The most significant factors affecting the nanoparticle size were silver nitrate concentration and pH [32]. The response surface methodology to optimize the synthesis of iron oxide (Fe_3O_4) nanoparticles and investigated the effects of various synthesis parameters such as temperature, reaction time, and precursor concentration. The research found the most significant factors affecting nanoparticle size were reaction temperature and reaction time [33]. The design of experiments (DOE) method to optimize the synthesis of zinc oxide nanoparticles via the sol-gel method [34]. The researchers conducted an investigation into the effects of zinc acetate concentration, ethanol volume, and milling time on the synthesis of nanoparticles. Among these parameters, the study revealed that zinc acetate concentration and milling time were the most influential factors in producing the nanoparticle size. The response surface methodology used to optimize the synthesis of gold nanoparticles via a solvothermal method. The effects the amount of reducing agent, reaction time, and reaction temperature was investigated [35]. Results confirmed that the most significant factors affecting nanoparticle size were reaction time and reaction temperature. Merida eta al. [36] used the Taguchi method to optimize the synthesis of iron oxide nanoparticles via the co-precipitation method. They considered the effects of various synthesis parameters such as pH, temperature, and stirring speed. Their study found that the most significant factors affecting nanoparticle size were pH and temperature.

Hence, the primary objective of this research article is to find best conditions for the mechanical milling process for synthesizing copper oxide and tin oxide nanoparticles with augmented antibacterial activity through the utilization of statistical analysis applied to experimental variables. By systematically manipulating key synthesis parameters, including composition, heating temperature, milling time, and reducing agent addition, the authors have successfully developed a robust methodology for the fabrication and design of copper-tin alloy nanoparticles exhibiting exceptional antibacterial properties. This novel and innovative approach exhibits the promise of transforming the realm of antibacterial nanoparticles and presenting a novel tool for combating drug-resistant bacterial strains.

2. Experimental work and design of experiments

2.1. Raw material and synthesis

In this study, the copper oxide used was sourced from the Pouyan Chemical Institute and boasted a purity level of 99.3%, with a particle size of roughly 100 μm. Similarly, the tin oxide used had a purity level of 99.6% and a particle size of approximately 80 μm. To aid in the milling and regeneration processes, a pre-milled mixture of polyethylene glycol and graphite with a purity level of 99.2% and particle size below 5 μm, respectively, was used as a surfactant. The use of graphite helped to prevent fine dust particles from clumping together and facilitated a higher quality milling operation. Alloys with varying proportions of both elements were produced based on previous research study [3], as detailed in **Table 1**. The amount of material used in the experiment was determined through the application of **Equation (1)** based on thermodynamic analysis and regenerative reaction.

Table 1. Raw materials characteristics for this study.

Sample	Copper (wt%)	Tin (wt%)	polyethylene glycol (wt%)	Purity (%)	Particles Size (µm)
#1	35	65	2	99.6	60
#2	50	50	2	99.5	70
#3	85	15	2	99.3	80

$SnO_2+CuO+1.5C \rightarrow Sn-Cu+1.5CO_2$ ΔG_{298}=54.1 KJ/mol., ΔH_{298}=144.6KJ/mol (1)

The high-energy milling process in this study utilized a planetary ball mill, specifically the PM 2400 model (China), with two milling chambers. The milling operation commenced by measuring 7.56 grams of copper, 14.46 grams of tin, and 2.41 grams of graphite with a four-decimal balance, as per **Equations (1-3)**.

$SnO_2+C \rightarrow Sn+CO_2$ ΔG_{298}=157 KJ/mol., ΔH_{298}= -531.6 KJ/mol (2)

$CuO+0.5C \rightarrow Cu+0.5CO_2$ ΔG_{298}= 283 KJ/mol., ΔH_{298}= -952.9 KJ/mol (3)

A mixture of copper oxide and tin oxide powders, with 40% excess graphite to achieve oxide, carbide, alloying, and structural samples, was loaded into the milling chamber along with chromium steel bullets of two diameters: 9 and 14 mm. The milling process lasted for durations of 1 hour, 10 hours, and 30 hours, with a powder-to-bullet ratio of 1:20 and a milling speed of 120 rpm under an argon atmosphere, as detailed in **Table 2**. The use of oxide powders with both micron and millimeter dimensions ensured a more thorough crushing of powder particles on the nanometer scale. The powder mixtures produced were in varying proportions of raw materials, including 35%, 50%, and 85% copper. Input variables and output responses are shown in **Table 2**.

Table 2. Input variables process parameters with design levels.

Variable	Symbol	Units	-1	0	1
Cu composition (%)	**W**	%	35	50	85
Heating Temperature (°C)	**H**	°C	400	700	1000
Milling Time (h)	**T**	h	1	10	30

After it became evident that milling alone would not sufficiently activate the graphite powder mixture in a timely manner, it was decided to utilize heat treatment. A combination of all samples was subjected to heat treatment in alumina boats placed inside quartz reactors, at temperatures of 400, 700, and 1000°C for 1 hour, with a heating rate of 10°C per minute under an argon atmosphere. The heat treatment was carried out using an induction tube furnace. Prior to the actual heat treatment, a test was conducted to determine the necessary temperature levels, which ultimately helped to identify the suitable temperatures required for the heat treatment process.

2.3. Antibacterial experiments

A spectral machine was used to prepare a dilution of each sample with an optical density (O.D) concentration at a wavelength of 600 nm up to a final concentration of 105 cells/mL. Next, 2 mL of the bacterial dilution was added to the growth medium and nanoparticles using a 2 mL sampler. The same steps were taken to prepare the control group, with the exception of the addition of nanoparticles. The containers were then sealed and incubated in a shaker at 250 rpm at 37°C for 24 hours. The electron concentration was measured by an optical density of 600 nm, and the treatment and control environments were poured into glass coils for the OD. The dilution of nanoparticles in the bacterial growth medium was used to calibrate the spectrophotometer as a blank solution. In the pour plate method, a suspension of bacteria is prepared by diluting it in a liquid medium. One milliliter of the dilution is poured into the bottom of a sterile plate, followed by the addition of 20 mL of the desired culture medium previously sterilized and heated to around 45°C. The mixture is then thoroughly mixed in a circular motion. If a thin layer of the same culture medium is applied to the surface of the bacterial environment, it is known as a double-layer culture. After cultivation, different percentages of nanoparticles are added, and the colonies are counted with a colony counting

device after one day for each plate. The experiment is repeated for each sample, and the mean results are reported.

2.4. Methods of characterization

The morphology and phases of all Cu-Sn particles were investigated. XRD measurements were used to determine the new phases and particle size (Philips model Empyrean Alpha, Lelyweg, The Netherlands). A field emission scanning electron microscopy (FE-SEM) (MIRA3-TESCAN, Kohoutovice, Czech Republic) was also used to determine particle morphology and size confirmation. The differential thermal analysis (DTA) of nanoparticles was investigated using an adapted TGA-SDTA851e (Thermal system Mettler Toledo, Spain). To investigate the antibacterial properties of copper-tin nanoparticles against Gram-negative bacteria, E-coli the optical density method and colony counting were used. LB agar medium (consisting of tryptone 15g/l, sodium chloride 3g/l, yeast extract 3g/l, and agar 25g/l) was used to prepare the bacterial culture medium.

3. Results and discussion

Ball milling experiments were carried out according to the matrix design presented in **Table 3** in which an overview of the results of the experiments is illustrated. Based on the experimental data generated from laboratory testing conducted in accordance with the Design of Expert software guidelines, the resulting data was subjected to detailed analysis and further discourse.

Table 3. The design matrix of the three input process parameters and the three output responses

	Input variables (factors)			Output variables (responses)		
Sample	**Cu Composition (%)**	**Heating Temperature (C)**	**Milling Time (h)**	**Particle Size (nm)**	**Optical Density (600 nm)**	**Number of Colonies**
#1	50	1000	30	15	0.587	87
#2	85	400	10	28	0.534	95
#3	35	1000	10	36	0.171	298
#4	35	700	30	21	0.293	174
#5	50	400	30	18	0.489	104
#6	35	1000	30	23	0.268	190
#7	85	1000	30	19	0.787	64
#8	35	400	10	24	0.257	199

#9	85	700	30	21	0.712	71
#10	50	700	1	41	0.215	238
#11	35	400	1	48	0.128	398
#12	50	1000	10	31	0.284	180
#13	50	400	10	34	0.259	197
#14	50	400	1	46	0.191	267
#15	85	700	10	33	0.453	112
#16	85	700	1	51	0.293	174
#17	35	400	30	29	0.212	240
#18	50	700	10	31	0.284	180
#19	85	1000	10	28	0.534	95
#20	50	1000	1	48	0.183	278
#21	35	700	10	43	0.143	356
#22	85	1000	1	41	0.365	140
#23	85	400	1	47	0.318	160
#24	35	700	1	43	0.143	356
#25	85	400	30	21	0.712	71
#26	35	1000	1	49	0.126	406
#27	50	700	30	17	0.518	98

3.2. Identification of nanoparticle phases

3.2.1. X-ray diffraction (XRD)

Figure 1 shows the XRD patterns of the binary powder blends of the Cu85Sn15 sample obtained after 10 min. As-received and 30 h of ball milling under an Ar atmosphere in hardened steel vials. The preliminary experiments revealed that both phases fcc Cu and fcc Sn are still present after 30 h of ball milling. After 30 h the Cu and Sn peaks drop down and the diffraction patterns can be indexed to a single hcp phase, which suggests the formation of a Cu_3Sn solid solution of bimetallic nanoparticles. Cu_3Sn: This phase typically appears at around 44.3° 2-theta. Cu_3Sn phase has a tetragonal crystal structure with the lattice parameters a=0.4186 nm and c=0.3281 nm. The most intense peaks in the XRD pattern of Cu_3Sn correspond to the (101) and (200) planes.

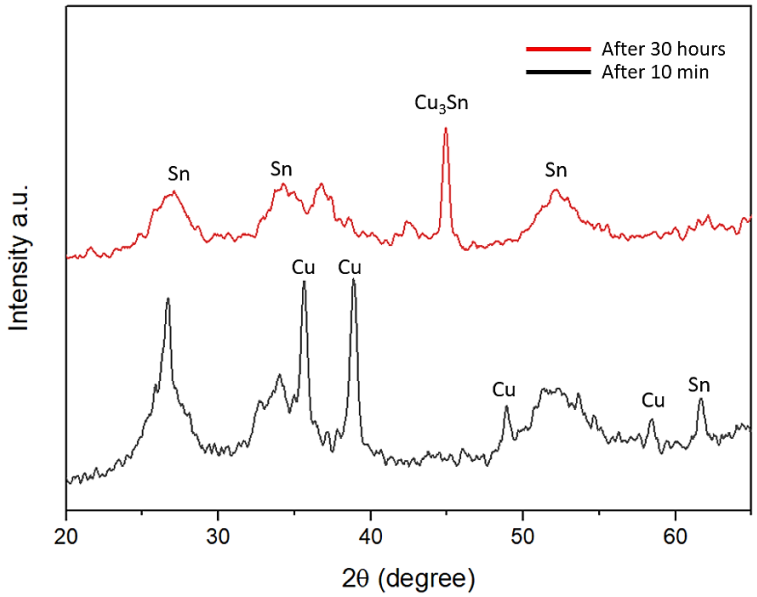

Figure 1. XRD patterns of CuSn samples for optimum milling time of 10 min and 30 h.

According to the phase diagram, these XRD results show the simple formation of CuSn alloys throughout the milling process, which is consistent with the complete solid solubility at room temperature for the Cu-Sn system [37,38]. As the Cu_3Sn (at%) content increases, the Bragg peaks shift to higher diffraction angles in both cases (101) and (200). The 2θ angles of the characteristic reflections corresponding to the (101) and (200) planes of bulk fcc metals are 36.47, 38.375, 48.54, 57.84 (Cu) and 27.8, 34.74, 52.43, 63.13 (Sn).

3.2.2. Differential thermal analysis (DTA)

Differential thermal analysis (DTA) was conducted on CuSn powder that was mechanically alloyed through ball milling to examine its thermal behavior. The DTA analysis diagrams (**Figure 2**) revealed that the CuSn alloy exhibited an endothermic peak at a temperature of approximately 700°C, 1000°C, which may be attributed to the formation of an intermetallic compound. Additionally, an exothermic peak was observed at around 400°C, which could be associated with the oxidation of the alloy or the crystallization of a new phase. Overall, the DTA results suggest that ball milling effectively produces a CuSn alloy with distinct thermal properties. Samples were subjected to heat treatment (reduction process) at

temperatures of 400°C, 700°C, and 1000°C, to investigate the formation of new CuSn phases and to facilitate further experimentation.

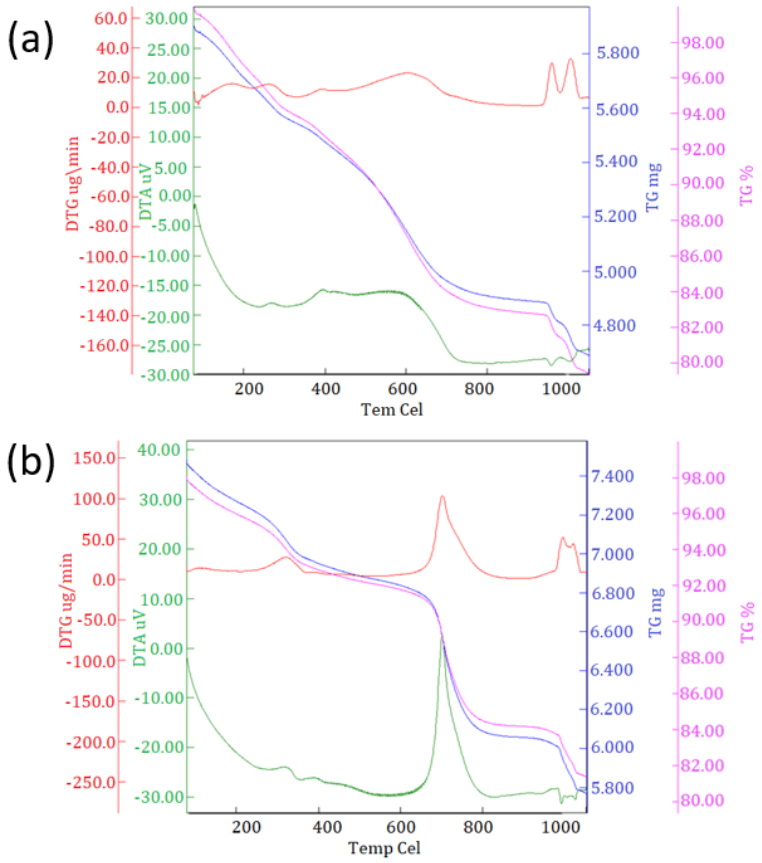

Figure 2. DTA diagrams of CuSn samples (a) after 10 min. ball milling and (b) after 30 h ball milling.

3.2. Particle size

Table 4 shows the ANOVA table for particle size after the milling ball mechanical alloying process. All input factors are significant in the final regression **Equation (4)**. The particle size of CuSn powder after 30 hours of milling using ball mechanical alloying can vary depending on several factors such as the milling parameters (e.g., milling speed, ball-to-powder ratio, milling time, etc.), the starting particle size, and the type of milling equipment used. However, typically, after 30 hours of milling using ball mechanical alloying, the CuSn powder should have undergone significant particle size reduction. The initial particle size of the starting CuSn powder and the milling parameters will determine the final particle size of the milled powder.

Table 4. ANOVA for particle size.

Source	Sum of Squares	df	Mean Square	F-value	p-value
Model	2035.05	6	339.18	21.13	< 0.0001
A-Cu Composition	15.27	1	15.27	0.9512	0.3472
B-Heating Temperature	0.1246	1	0.1246	0.0078	0.9311
C-Milling Time	1927.27	1	1927.27	120.05	< 0.0001
BC	34.22	1	34.22	2.13	0.1680
A^2	37.38	1	37.38	2.33	0.1510
C^2	307.03	1	307.03	19.13	0.0008
Lack of fit	203.15	8	0.037		
Pure error	0.037	5	7.822E−003		
Residual	208.70	13	16.05		
	R-Squared = %86.41			*R-Squared (Adj) =%78.06*	

$$\text{Particle Size} = +21.60 - 1.17\,A + 0.0970\,B - 13.53\,C - 2.03\,BC + 3.31\,A^2 + 10.14C^2 \quad (4)$$

In general, the milling process involves repeated cold welding, fracturing, and re-welding of the powder particles due to the impact of the milling balls [39,40] .As the milling process progresses, the powder particles undergo deformation and fracture, reducing particle size. **Figure 3** displays the normal probability plot to analyze the percentage of particle size distribution after mechanical alloying via ball milling. This statistical tool enables the visual assessment of the normality assumption of the data and identifies any deviations from the expected normal distribution. The analysis of the normal probability plot revealed a linear trend with a high R-squared value, suggesting that the data closely follows a normal distribution. Therefore, it can be concluded that the particle size distribution data obtained after mechanical alloying via ball milling can be treated as normally distributed. The predict vs. actual plot was used to analyze the accuracy of the prediction model for the particle size distribution data obtained after mechanical alloying via ball milling. The predicted values were generated using a regression model, while the actual values were obtained through experimental measurements. The analysis of the predict vs. actual plot revealed a high degree of correlation between the predicted and actual values, with a slope close to 1 and a low intercept value. This indicates that the prediction model is highly accurate in estimating the particle size distribution after mechanical alloying via ball milling. Therefore, the model can be reliably used for future predictions of particle size distribution under similar experimental conditions.

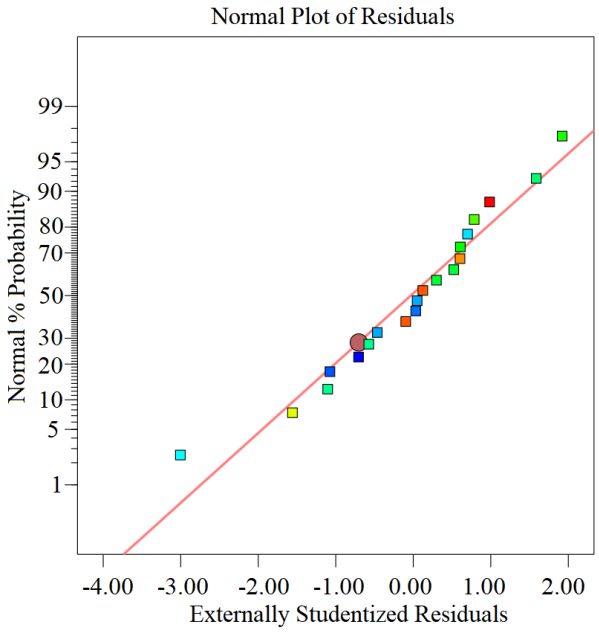

Figure 3. Statistical plot for particle size as the response.

Perturbation plot **Figure 4** was employed to investigate the effect of individual observations on the model prediction for the particle size distribution data obtained after mechanical alloying via ball milling. The perturbation plot displays the influence of each observation on the predicted values, with larger points representing observations that exert a greater influence on the model prediction. The analysis of the perturbation plot indicated that a few observations had a significant impact on the model prediction, with some observations exerting a larger influence on the predicted values than others. These observations can be further investigated to determine their root causes and refine the experimental methodology for improving the model prediction accuracy. Overall, the perturbation plot provides a useful tool for identifying influential observations and improving the accuracy of the prediction model. The results indicate that Cu composition (%), heating temperature (°C), and milling time (h) are statistically significant factors in the observed response variable (particle size). This suggests that changes in these factors have a significant impact on the particle size distribution after mechanical alloying via ball milling. These factors can be further investigated to achieve

the desired particle size distribution and enhance the overall efficiency of the mechanical alloying process.

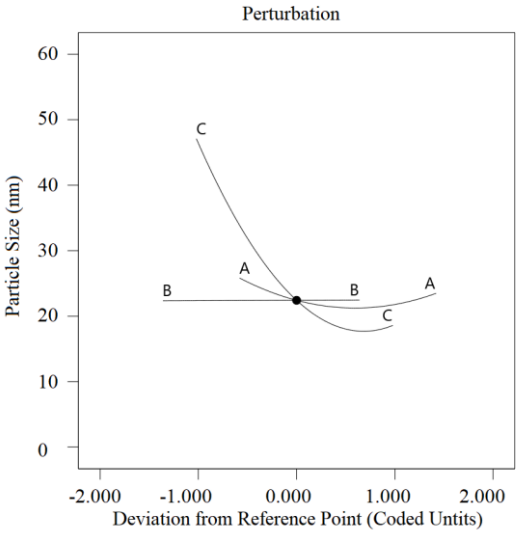

Figure 4. Perturbation plot for particle size after 30 h ball milling.

The 3d surface plot (**Figure 5**) was utilized to investigate the effect of heating temperature (°C) and milling time (h) on particle size distribution after mechanical alloying via ball milling, while holding Cu composition (%) constant. The plot revealed that Cu composition (%) was not a significant factor in determining particle size distribution. However, heating temperature (°C) had a significant effect, with higher temperatures decreasing particle size. Additionally, the effect of milling time (h) on particle size was observed to be nonlinear, with increasing milling time leading to a decrease in particle size until nanoparticles were formed. The 3d surface plot provides a useful visualization of the complex relationship between heating temperature, milling time, and particle size distribution after mechanical alloying via ball milling. This information can be used for the process parameters to achieve the desired particle size distribution and to enhance the efficiency of the mechanical alloying process. Overall, the 3d surface plot is a powerful tool for investigating the impact of multiple factors on the response variable and for identifying the conditions for a given process.

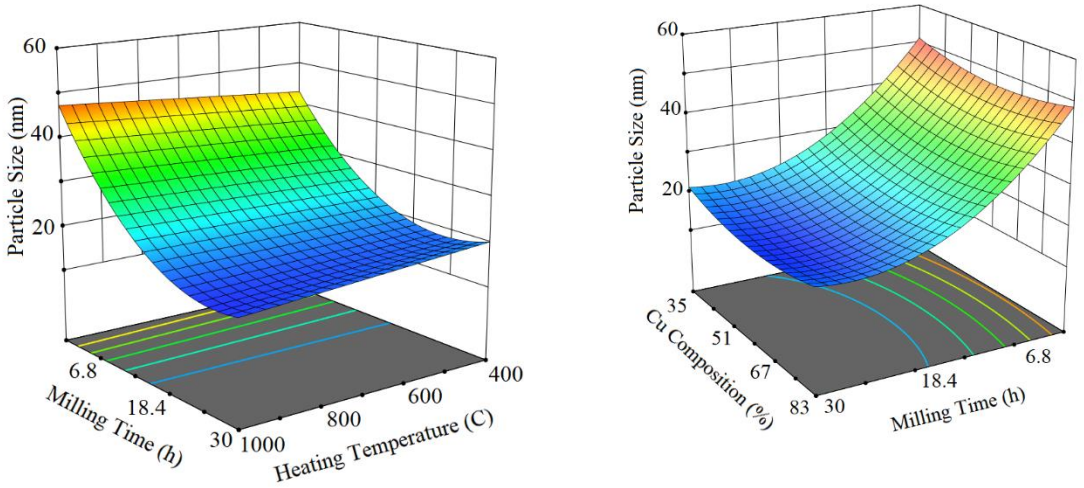

Figure 5. 3d surface plot for all input factors versus particle size as the response.

Field emission electron micrographs for the mechanically synthesized Cu–Sn nanoparticles of the sample (#3) are shown in **Figure 6**.

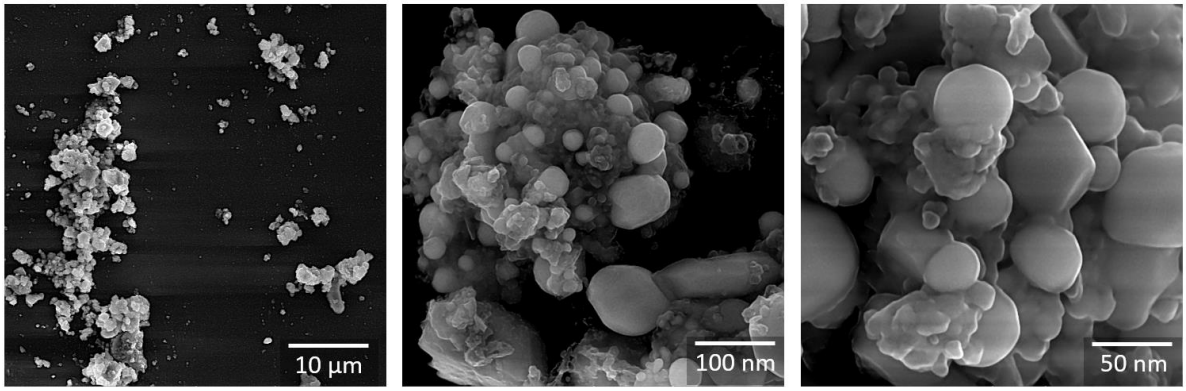

Figure 6. FE/SEM micrograph of mechanically alloyed CuSn particles (sample #3).

The particles are partially agglomerated; some reasons for this are the high surface energy of nanoparticles, which can lead to agglomeration or clustering. Additionally, the nanoparticles can undergo plastic deformation during the mechanical milling process, causing them to stick together. The presence of impurities or incomplete reduction of precursor materials can also contribute to agglomeration. Furthermore, inadequate milling conditions, such as high milling speeds or prolonged milling times, can also lead to agglomeration. Optimizing the milling conditions to prevent excessive deformation and agglomeration of the nanoparticles is essential, with some larger grains in the shape of spheres 50 nm visible (sample #3) (see **Figure**

6). However, after examining the sample, it was determined that these particles were relatively small. Because polyethene glycol normally prevents agglomeration, the effect of polyethene glycol on nanoparticle agglomeration was investigated. Milling samples increases the specific area on one side; however, samples reacted with the oxygen present for oxidation protection due to the relatively large specific surface area. Oxides may contaminate the milled sample if oxygen penetrates the sealed vial during the long milling period. As a result, the best milling time in sample milling appears to be around 20 seconds. One potential observation from SEM images is the particle size distribution. After mechanical alloying process the particle size reducing, the SEM images show a narrower size distribution of smaller particles compared to the initial powder mixture. Alternatively, if the milling process was insufficient or excessive, the SEM images may show a wide range of particle sizes or particles that have aggregated. Another potential observation from SEM images is the particle shape. The particles appear more uniform in shape, possibly with a spherical or irregular shape due to the collision between the milling balls and the powder particles. In contrast, if the milling process was insufficient, the particles may appear more angular with sharp edges and corners. The FE/SEM images demonstrate the presence of grains and the distribution of the phases. The SEM images show a more homogeneous microstructure with smaller grain sizes than the initial powder mixture. From FE/SEM images can also reveal the surface morphology of the CuSn powder, including the presence of surface defects, such as cracks, pores, and grain boundaries. The surface morphology can affect the material's reactivity and can also influence its interactions with other materials, or in the case of antibacterial properties, it can absorb more bacteria when it’s in the culture plate.

3.3. Antibacterial activity

3.3.1. Optical density

The ANOVA table for optical density as antibacterial test after milling ball mechanical alloying process shown in **Table 5**. All input factors are significant in the final regression

Equation (5), and as the p-value of AC (A-Cu Composition * C-Milling Time) is less than 0.05 its significant on the optical density experiments.

Table 5. ANOVA for optical density.

Source	Sum of Squares	df	Mean Square	F-value	p-value
Model	0.6509	7	0.0930	31.92	< 0.0001
A-Cu Composition	0.3291	1	0.3291	113.00	< 0.0001
B-Heating Temperature	0.0004	1	0.0004	0.1506	0.7048
C-Milling Time	0.2555	1	0.2555	87.72	< 0.0001
AC	0.0229	1	0.0229	7.87	0.0159
BC	0.0045	1	0.0045	1.55	0.2371
A^2	0.0067	1	0.0067	2.28	0.1565
B^2	0.0045	1	0.0045	1.56	0.2355
Lack of fit	0.0350	9	0.0047		
Pure error	0.000	5	6.451E−002		
Residual	0.0350	12	0.0029		
	R-Squared = %91.93			*R-Squared (Adj) =%84.77*	

$$\text{Optical Density} = +0.3931 +0.1790\ A +0.0058\ B +0.1500\ C +0.0549\ AC +0.0240\ BC -0.0444\ A^2 +0.0350\ B^2 \quad (5)$$

The normal plot of residuals (**Figure 7**) is a graphical method for evaluating whether the residuals of a statistical model are normally distributed. The normal probability plot shows the theoretical quantiles of the normal distribution on the x-axis and the observed quantiles of the residuals on the y-axis. If the residuals are normally distributed, the points on the plot should follow a straight line. In addition, the externally studentized residuals are the residuals that are divided by their estimated standard deviation. They are useful for detecting influential observations or outliers that may greatly impact the regression results. Based on the given information, the normal plot of residuals can be interpreted as follows: The maximum externally studentized residual is 0.787, which means that one observation has a large influence on the regression results. This observation may be an outlier or have a large leverage on the regression line. The minimum externally studentized residual is 0.128, which is not particularly low or high compared to the other residuals. Regarding the normal probability plot, if the points fall along a straight line, we can assume that the residuals are normally distributed. However, without knowing the number of observations or the number of predictors in the regression

model, it is difficult to provide a more detailed analysis of the plot. The residuals versus predicted plot is a graphical method for evaluating the assumption of homoscedasticity, which means that the variance of the residuals should be constant across all levels of the predictor variable. In this plot, the residuals are plotted against the predicted values of the response variable. If there is a clear pattern in the plot, it suggests that the variance of the residuals is not constant and may violate the assumption of homoscedasticity. The externally studentized residuals are the residuals that are divided by their estimated standard deviation. They are useful for detecting influential observations or outliers that may have a large impact on the regression results. Based on the given information, we can interpret the residuals versus predicted plot as follows: If there is a clear pattern in the plot, such as a funnel shape, a curve, or a U-shape, it suggests that the variance of the residuals is not constant. This may be due to a violation of the assumption of homoscedasticity or the presence of outliers or influential observations. If the plot appears to be random, with no clear pattern, it suggests that the variance of the residuals is approximately constant across all levels of the predictor variable, and the assumption of homoscedasticity may be reasonable. The externally studentized residuals can help identify influential observations or outliers that may be driving any patterns in the plot. If there are any points with high externally studentized residuals, it may indicate that these observations are having a large impact on the regression results and should be investigated further. In terms of the predicted versus externally studentized residuals plot, this plot shows how influential observations or outliers relate to the predicted values of the response variable. Suppose there are any points with high externally studentized residuals and high predicted values. In that case, it may indicate that these observations are driving the model results at high levels of the predictor variable.

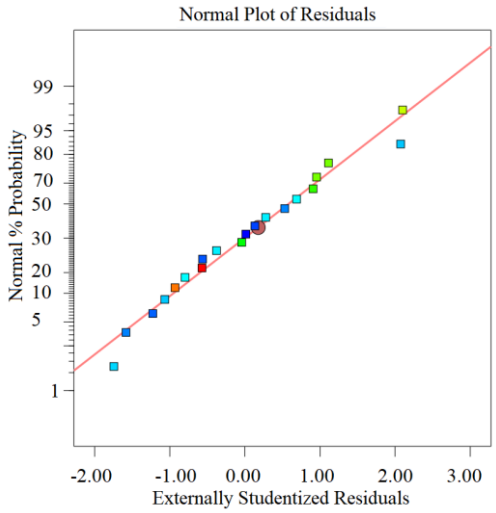

Figure 7. Statistical plot for optical density as the response.

A contour plot (**Figure 8**) is a type of graphical representation used to visualize a three-dimensional surface (**Figure 9**) by displaying the constant values of a response variable on a two-dimensional plot. In this case, the response variable is the optical density, and the two-dimensional plot displays the Cu composition and optical density values. Based on the given information, the contour plot shows that as the Cu composition increases, the optical density also increases. This suggests that there is a positive correlation between Cu composition and optical density, indicating that increasing the Cu composition in the material is likely to result in an increase in optical density. This relationship may be useful in designing and optimizing materials for specific optical properties. For example, if a higher optical density is desired, increasing the Cu composition may be a viable approach to achieve that goal. It is important to note that while the contour plot shows a positive correlation between Cu composition and optical density, other factors may also influence the optical properties of the material. It may be necessary to consider other variables or factors in conjunction with the Cu composition to fully understand the relationship for a specific application.

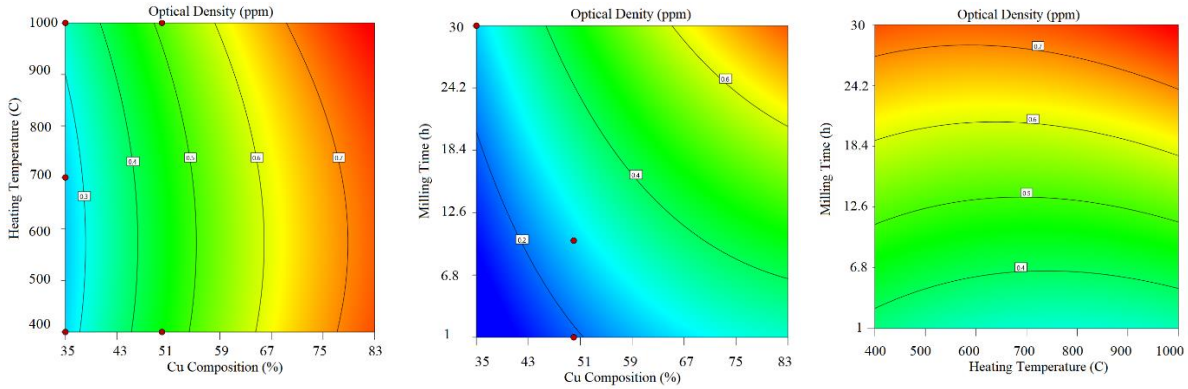

Figure 8. Contour plot for optical density.

Based on the given information, the contour plot shows that as the milling time increases, the optical density also increases. This suggests that there is a positive correlation between milling time and optical density, indicating that increasing the milling time in the material is likely to result in an increase in optical density. This relationship may be useful in designing materials for specific optical properties, especially if the milling time can be controlled in the manufacturing process. For example, if a higher optical density is desired, increasing the milling time may be a viable approach to achieve that goal. It is important to note that while the contour plot shows a positive correlation between milling time and optical density, other factors may also influence the optical properties of the material. It may be necessary to consider other variables or factors in conjunction with milling time to fully understand the relationship for a specific application. The Surface plot (**Figure 9**) shows that the heating temperature does not affect the optical density. This suggests that there is no correlation between heating temperature and optical density, indicating that increasing or decreasing the heating temperature in the material does not have an effect on the optical density. While this may seem like a negative result, it can still be useful information in designing and optimizing materials for specific properties. If Heating Temperature does not affect the optical density, then the material can be heated or cooled to a range of temperatures without impacting its optical properties. This may be beneficial in manufacturing processes where temperature control is necessary for other aspects of the material. It is important to note that while the contour plot

shows no correlation between Heating Temperature and optical density, other factors may still impact the optical properties of the material. It may be necessary to consider other variables or factors in conjunction with heating temperature to fully understand the relationship a specific application.

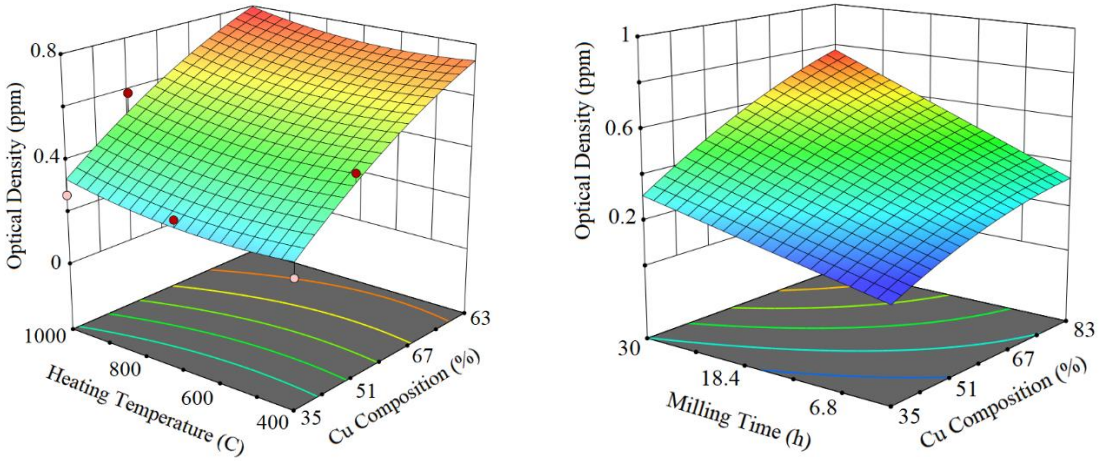

Figure 9. 3d surface plots for interaction between all input factors and responses.

The optical density diagram is shown in **Figure 10** and provides a useful visualization of the antibacterial activity of CuSn nanoparticles powder. The diagrams show the optical density of the medium culture of bacteria when exposed to Cu35Sn65, Cu50Sn50, and Cu85Sn15 nanoparticles at a concentration of 100 ppm and the transmission of 600 nm light through the medium culture of bacteria. The diagram shows that Cu85Sn15 nanoparticles have better antibacterial properties compared to Cu35Sn65 and Cu50Sn50 nanoparticles. This suggests that the CuSn nanoparticles with a higher concentration of Sn (85%) and a lower concentration of Cu (15%) may be more effective in inhibiting bacterial growth. In addition, the diagram also shows that the transmission of 600 nm light passes more easily through the medium culture of bacteria when exposed to Cu85Sn15 nanoparticles compared to Cu35Sn65 and Cu50Sn50 nanoparticles. This may indicate that the Cu85Sn15 nanoparticles are more transparent and have a lower scattering effect on light, which may have implications for their potential use in antibacterial applications.

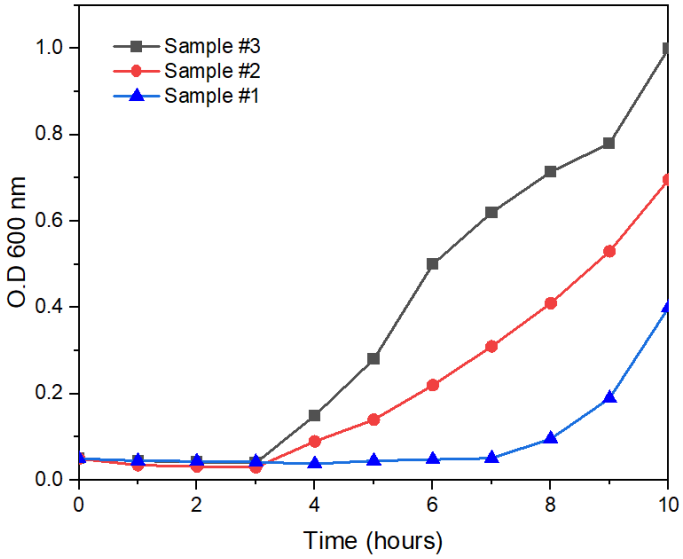

Figure 10. Optical density diagrams for antibacterial activity.

3.3.2. Colony forming units counting (CFU)

Table 6 shows the analysis of variance for CFU with all terms as sources. As explicated in the previous sections, a significant level of less than α=0.05 has been identified. Regarding CFU, both Cu composition and milling time exhibit α values below 0.05, suggesting that they may exert an impact on the final regression **Equation 6**.

Table 6. ANOVA for colony forming units counting.

Source	Sum of Squares	df	Mean Square	F-value	p-value
Model	1.332E+05	6	22195.58	24.73	< 0.0001
A-Cu Composition	72985.00	1	72985.00	81.31	< 0.0001
B-Heating Temperature	0.0157	1	0.0157	0.0000	0.9967
C-Milling Time	54984.95	1	54984.95	61.26	< 0.0001
AC	2081.06	1	2081.06	2.32	0.1518
A^2	9736.00	1	9736.00	10.85	0.0058
C^2	8740.92	1	8740.92	9.74	0.0081
Lack of fit	226.4	8	15.73		
Pure error	9.425E−003	5	4.461E−003		
Residual	199.46	10	19.95		
	R-Squared = %86.78			*R-Squared (Adj) =%75.89*	

$$\text{Number of Colonies} = +95.97 - 81.22\,A - 0.0345\,B - 73.81\,C + 15.80\,AC + 53.28\,A^2 + 53.60\,C^2 \quad (6)$$

The plots (**Figure 11 a and b**) show the number of colonies of bacteria as a function of both the Cu composition and milling time of the nanoparticles. Based on the information provided, the 3d surface plot and contour plot indicate that as the Cu composition and milling time of the nanoparticles increase, the number of colonies of bacteria reduces. The reduction in the number of colonies continues until it reaches less than 100, indicating a significant

antibacterial effect. The plots suggest that increasing the Cu composition and milling time of the nanoparticles may increase their antibacterial activity, potentially making them effective in inhibiting bacterial growth. This may have important implications for the development of new antibacterial agents and the design of materials with enhanced antibacterial properties. It is important to note that while the 3d surface plot and contour plot provide valuable insights into the relationship between Cu composition, milling time, and antibacterial activity, other factors may also impact the antibacterial properties of the nanoparticles. It may be necessary to consider other variables or factors in conjunction with Cu composition and milling time to fully understand the relationship of the nanoparticles for an antibacterial application.

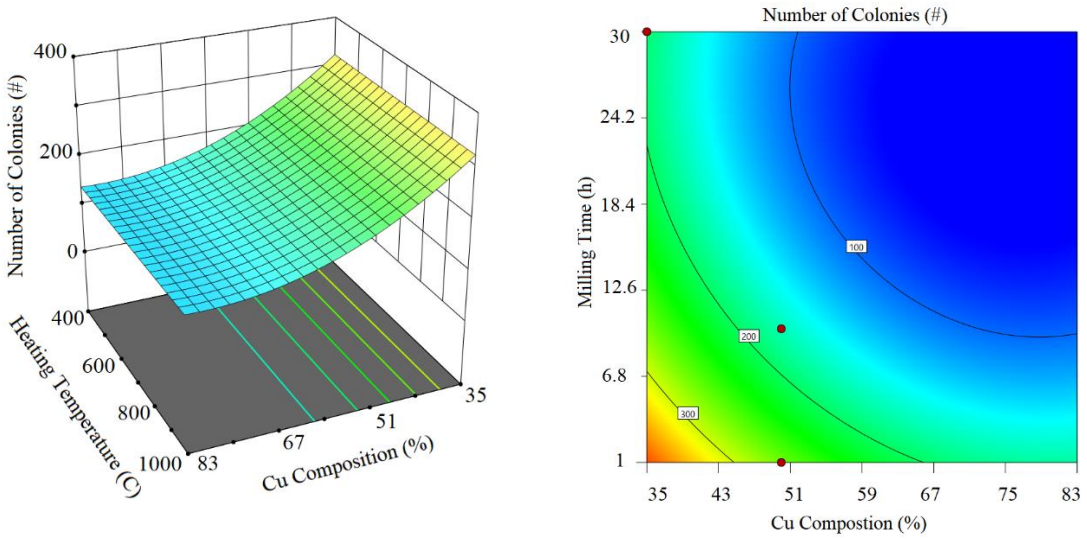

(a) (b)

Figure 11. (a) 3d surface plot, (b) contour plot for the number of colonies.

In the case of the antibacterial activity of CuSn nanoparticles powder, the plots show that increasing the Cu composition and milling time of the nanoparticles results in a decrease in the number of bacterial colonies. This reduction in bacterial colonies is a significant result as it suggests that the nanoparticles may be effective at inhibiting bacterial growth. The reduction in bacterial colonies observed in the 3d surface plot and contour plot may be due to several factors. For example, the increased Cu composition may lead to the release of copper ions, which have been shown to have antibacterial properties. The increased milling time may also

result in a reduction in particle size and an increase in surface area, which may enhance the antibacterial properties of the nanoparticles. It is important to note that the 3d surface plot and contour plot provide a visualization of a complex relationship between variables and that other factors may also impact the antibacterial properties of the nanoparticles. Further research and analysis may be needed to fully understand the relationship between Cu composition, milling time, and antibacterial activity and to find the properties of the nanoparticles for a specific application.

Figure 12 demonstrates the liquid environment with Escherichia coli bacteria and nanoparticles of sample #3 with 85% Cu composition. The amount of 2.75 mg of sample #3 as an antibacterial nanoparticle was added to this medium culture plate, and the results after 24, 48, and 72 hours were analysed. The statement indicates that a sample (#3) of an antibacterial nanoparticle containing 85% Cu composition was added to a medium culture plate containing Escherichia coli bacteria. The amount of the sample added was 2.75 mg. The results of the experiment were analyzed at 24, 48, and 72 hours after the addition of the sample.

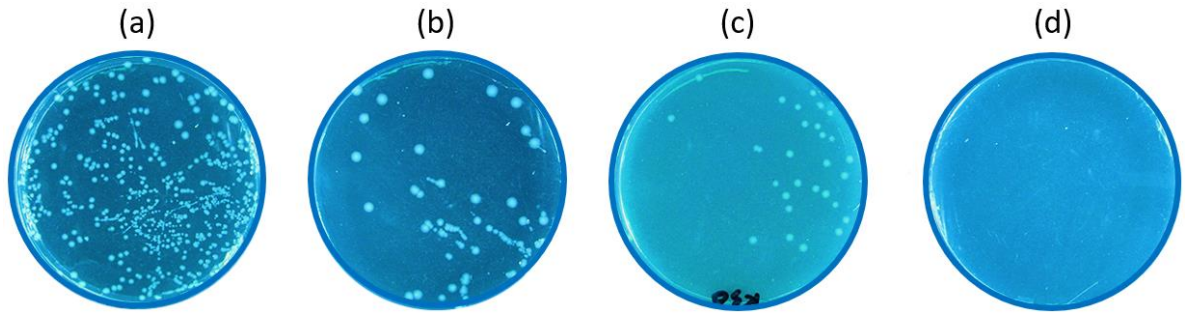

Figure 12. medium culture bacteria plates for Colony forming units counting for sample #3, (a) without nanoparticles, (b) after 24 hours, (c) after 48 hours, (d) after 72 hours.

The analysis of the results revealed that after 72 hours, there were almost no bacterial colonies present in the liquid environment medium culture of Escherichia coli bacteria. This result advocates that the sample of the antibacterial nanoparticle was effective at inhibiting the growth of Escherichia coli bacteria. The effectiveness of the sample may be attributed to the presence of copper ions, which have been shown to have antibacterial properties [41]. The high

Cu composition of the sample (#3) may have resulted in a higher release of copper ions, which could have enhanced its antibacterial properties. It is important to note that the experiment was conducted under controlled conditions, and further research may be necessary to validate the results and to determine the best conditions for using the antibacterial nanoparticle as a potential agent for inhibiting the growth of bacteria. The statement suggests that the antibacterial nano powder may be effective at destroying the bacterial membrane shell. The bacterial membrane shell is a crucial component of bacterial cells, as it serves to protect the cell from external threats, such as toxins and other harmful substances [42]. The mechanism of action of the antibacterial nano powder may involve the release of copper ions, which have been shown to have antibacterial properties. These copper ions may disrupt the integrity of the bacterial membrane shell, leading to the destruction of the bacterial cell. The antibacterial nano powder also be able to penetrate the cell membrane and disrupt the intracellular components of the bacterial cell, further contributing to its antibacterial effects. Destroying the bacterial membrane shell may depend on various factors, including the composition and structure of the nano powder, as well as the type of bacteria being targeted. Additionally, the concentration of the nano powder and the duration of exposure may also affect its effectiveness.

Conclusion

In this study, input variables (Cu Composition (%), Heating Temperature (C), Milling Time (h)) with three output responses (Particle Size (nm), Optical Density (ppm), and Number of Colonies) were investigated with the design of experiments technic. The results show that all input factors are significant on final nanoparticle production.

1. Mechanical alloying produced nanoparticle powders up to 15 nanometers in size. DTA revealed disturbances at 400, 700, and 1000 °C, indicating the presence of new phases. XRD confirmed the presence of Cu_3Sn phases in the final nanoparticle structure.

2. The three input variables directly influenced grain size, and the optical density test revealed that increasing the percentage of copper in the alloy resulted in greater light transmission, indicating enhanced antibacterial properties.
3. The three-dimensional graph displayed a decrease in the number of colonies with an increasing copper percentage in the alloy, illustrating the potent antibacterial properties of the alloy containing 85% copper. Furthermore, the bacterial colony count test demonstrated minimal impact on colonies after 72 hours when copper-tin alloy nanoparticles were introduced to the bacterial culture medium.

Statements & Declarations

Funding

The authors declare that no funds, grants, or other financial support were received during the preparation of this manuscript.

Competing Interests

The authors have no relevant financial or non-financial interests to disclose.

Data Availability

All data will be provided upon request from the corresponding authors.

Ethics Approval

Not applicable.

Consent to Participate

Not applicable.

Consent for Publication

All authors read and approved the final manuscript for publication.

Author Contributions

All authors contributed to the study conception and design. Material preparation, data collection and analysis were performed by M.R. The first draft of the manuscript was written by M.R and all authors commented on previous versions of the manuscript.

Acknowledgement

The authors respectfully acknowledge the technical support provided by Razi Foundation for laboratory equipment.

References

[1] G. Vimbela, S.M. Ngo, C. Fraze, L. Yang, D.A. Stout, Antibacterial properties and toxicity from metallic nanomaterials, Int J Nanomedicine. Volume 12 (2017) 3941–3965. https://doi.org/10.2147/ijn.s134526.

[2] J. Aien, A.A. Khan, S. Haq, A.R. Khan, K. Elmnasri, M. Ben Ali, M.S. AL-Harbi, M.I. Alghonaim, S.A. Alsalamah, A.A. Qurtam, F. Boufahja, A. Hedfi, M. Dellali, Antibacterial, Antioxidant and Physicochemical Properties of Pipper nigram Aided Copper Oxide Nanoparticles, Crystals (Basel). 13 (2023) 330. https://doi.org/10.3390/cryst13020330.

[3] M. Rezayat, M. Yazdi, M. Noghani, R. Ahmadi, Bactericidal Properties of Copper-Tin Nanoparticles on Escherichia coli in a Liquid Environment, Plasma. 3 (2020) 153–165.

[4] G. Strnad, L. Jakab-Farkas, F.S. Gobber, I. Peter, Synthesis and Characterization of Nanostructured Oxide Layers on Ti-Nb-Zr-Ta and Ti-Nb-Zr-Fe Biomedical Alloys, J Funct Biomater. 14 (2023) 180. https://doi.org/10.3390/jfb14040180.

[5] H.A. Rudayni, M.H. Shemy, M. Aladwani, L.M. Alneghery, G.M. Abu-Taweel, A.A. Allam, M.R. Abukhadra, S. Bellucci, Synthesis and Biological Activity Evaluations of Green ZnO-Decorated Acid-Activated Bentonite-Mediated Curcumin Extract (ZnO@CU/BE) as Antioxidant and Antidiabetic Agents, J Funct Biomater. 14 (2023) 198. https://doi.org/10.3390/jfb14040198.

[6] A. Azam, Size-dependent antimicrobial properties of CuO nanoparticles against Gram-positive and -negative bacterial strains, Int J Nanomedicine. (2012) 3527. https://doi.org/10.2147/ijn.s29020.

[7] M. Saghafi Yazdi, M. Rezayat, J.J.R. Rovira, ElectroCatalytic Activity of Nickel Foam with Co, Mo, and Ni Phosphide Nanostructures, Plasma. 5 (2022) 221–232. https://doi.org/10.3390/plasma5020017.

[8] S. Chatterjee, A. Bandyopadhyay, K. Sarkar, Effect of iron oxide and gold nanoparticles on bacterial growth leading towards biological application, J Nanobiotechnology. 9 (2011) 34. https://doi.org/10.1186/1477-3155-9-34.

[9] D.C. Duran, L.M. Gogan, A. Artene, V. Duran, The Components of Sustainable Development - a Possible Approach, Procedia Economics and Finance. 26 (2015) 806–811. https://doi.org/10.1016/s2212-5671(15)00849-7.

[10] Y.T. Gebreslassie, H.G. Gebretnsae, Green and Cost-Effective Synthesis of Tin Oxide Nanoparticles: A Review on the Synthesis Methodologies, Mechanism of Formation, and Their Potential Applications, Nanoscale Res Lett. 16 (2021). https://doi.org/10.1186/s11671-021-03555-6.

[11] M. Gautam, J.O. Kim, C.S. Yong, Fabrication of aerosol-based nanoparticles and their applications in biomedical fields, J Pharm Investig. 51 (2021) 361–375. https://doi.org/10.1007/s40005-021-00523-1.

[12] M. Rezayat, M.S. Yazdi, M.D. Zandi, A. Azami, Tribological and corrosion performance of electrodeposited Ni-Fe/Al2O3 coating, Results in Surfaces and Interfaces. (2022) 100083. https://doi.org/10.1016/j.rsurfi.2022.100083.

[13] A. Khatua, K. Kumari, D. Khatak, A. Roy, N. Bhatt, B. Paul, A. Naik, A.K. Patel, U.K. Panigrahi, S.K. Sahu, M. Saravanan, R. Meena, Synthesis and Spectral Characterisation of Fabricated Cerium-Doped Magnesium Oxide Nanoparticles: Evaluation of the Antimicrobial Potential and Its Membranolytic Activity through Large Unilamellar Vesicles, J Funct Biomater. 14 (2023) 112. https://doi.org/10.3390/jfb14020112.

[14] H. Jiang, Z. Ling, Y. Zhang, H. Mao, Z. Ma, Y. Yin, W. Wang, W. Tang, Z. Tan, J. Shi, L. Li, B. Ruan, Altered fecal microbiota composition in patients with major depressive disorder, Brain Behav Immun. 48 (2015) 186–194. https://doi.org/10.1016/j.bbi.2015.03.016.

[15] T. Li, Y. Lu, H. Zhang, L. Wang, R.C. Beier, Y. Jin, W. Wang, H. Li, X. Hou, Antibacterial Activity and Membrane-Targeting Mechanism of Aloe-Emodin Against Staphylococcus epidermidis, Front Microbiol. 12 (2021). https://doi.org/10.3389/fmicb.2021.621866.

[16] M. Moradi, M.K. Moghadam, M. Shamsborhan, Z.M. Beiranvand, A. Rasouli, M. Vahdati, A. Bakhtiari, M. Bodaghi, Simulation, statistical modeling, and optimization of CO2 laser cutting process of polycarbonate sheets, Optik (Stuttg). (2020) 164932. https://doi.org/10.1016/j.ijleo.2020.164932.

[17] A. Hasani, M. Azadbeh, M. Moradi, Sintering Process of Cu–28Zn Brass Alloy: Statistical Investigation, Transactions of the Indian Institute of Metals. 73 (2020) 1383–1400. https://doi.org/10.1007/s12666-020-01982-0.

[18] M. Moradi, M. KaramiMoghadam, High power diode laser surface hardening of AISI 4130; statistical modelling and optimization, Opt Laser Technol. 111 (2019) 554–570. https://doi.org/10.1016/j.optlastec.2018.10.043.

[19] A. Bahloul, C. Brochot, P. Abdolghader, F. Haghighat, Development of a procedure to measure the performance of ventilation filters for nanoparticles, IOP Conf Ser Mater Sci Eng. 609 (2019) 32032. https://doi.org/10.1088/1757-899x/609/3/032032.

[20] X. Dong, B. Milholland, J. Vijg, Dong et al. reply, Nature. 546 (2017) E7–E7. https://doi.org/10.1038/nature22785.

[21] V.K. Moghaddam, A.S. Dickerson, E. Bazrafshan, S.N. Seyedhasani, F. Najafi, M. Hadei, J. Momeni, G. Moradi, M. Sarmadi, Socioeconomic determinants of global distribution of multiple sclerosis: an ecological investigation based on Global Burden of Disease data, BMC Neurol. 21 (2021). https://doi.org/10.1186/s12883-021-02170-3.

[22] R. Mirzaei, P. Goodarzi, M. Asadi, A. Soltani, H.A.A. Aljanabi, A.S. Jeda, S. Dashtbin, S. Jalalifar, R. Mohammadzadeh, A. Teimoori, K. Tari, M. Salari, S. Ghiasvand, S. Kazemi, R. Yousefimashouf, H. Keyvani, S. Karampoor, Bacterial co-infections with SARS-CoV-2, IUBMB Life. 72 (2020) 2097–2111. https://doi.org/10.1002/iub.2356.

[23] R. Kaur, J.R. Labins, S.S. Helbock, W. Jiang, K.J. Bein, Q. Zhang, C. Anastasio, Photooxidants from brown carbon and other chromophores in illuminated particle extracts, Atmos Chem Phys. 19 (2019) 6579–6594. https://doi.org/10.5194/acp-19-6579-2019.

[24] N. Guemmoud, A. Hafs, T. Hafs, Effect of milling time on the structural, microstructure, and magnetic properties of nanocrystalline Fe90Sb10 powders obtained by high-energy ball milling, The International Journal of Advanced Manufacturing Technology. 122 (2022) 2043–2058. https://doi.org/10.1007/s00170-022-10003-x.

[25] J. Amiri Moghaddam, T. Jautzus, M. Alanjary, C. Beemelmanns, Recent highlights of biosynthetic studies on marine natural products, Org Biomol Chem. 19 (2021) 123–140. https://doi.org/10.1039/d0ob01677b.

[26] M.S. Akhtar, D. Chauhan, D. Ghosal, S. Poria, A. Ekbal, P. Bhattacharyya, Multi-task Learning for Multi-modal Emotion Recognition and Sentiment Analysis, Proceedings of the 2019 Conference of the North. (2019). https://doi.org/10.18653/v1/n19-1034.

[27] V. Calvo, J.M. González-Domínguez, A.M. Benito, W.K. Maser, Synthesis and Processing of Nanomaterials Mediated by Living Organisms, Angewandte Chemie International Edition. 61 (2021). https://doi.org/10.1002/anie.202113286.

[28] S. Paulose, R. Raghavan, B.K. George, Functionalized white graphene – Copper oxide nanocomposite: Synthesis, characterization and application as catalyst for thermal decomposition of ammonium perchlorate, J Colloid Interface Sci. 494 (2017) 64–73. https://doi.org/10.1016/j.jcis.2017.01.065.

[29] M. Zhu, L. Xu, L. Du, Y. An, C. Wan, Palladium Supported on Carbon Nanotubes as a High-Performance Catalyst for the Dehydrogenation of Dodecahydro-N-ethylcarbazole, Catalysts. 8 (2018) 638. https://doi.org/10.3390/catal8120638.

[30] S. Alam, M.S. Khan, A. Umar, R. Khattak, N. ur Rahman, I. Zekker, J. Burlakovs, S.S. dC Rubin, M.M. Ghangrekar, G.D. Bhowmick, A. Kallistova, N. Pimenov, A. Khan, M. Zahoor, Preparation of Pd–Ni Nanoparticles Supported on Activated Carbon for Efficient Removal of Basic Blue 3 from Water, Water (Basel). 13 (2021) 1211. https://doi.org/10.3390/w13091211.

[31] J. Arun, S. Nachiappan, G. Rangarajan, R.P. Alagappan, K.P. Gopinath, E. Lichtfouse, Synthesis and application of titanium dioxide photocatalysis for energy, decontamination and viral disinfection: a review, Environ Chem Lett. (2022). https://doi.org/10.1007/s10311-022-01503-z.

[32] L.A. Laime-Oviedo, A.A. Soncco-Ccahui, G. Peralta-Alarcon, C.A. Arenas-Chávez, J.L. Pineda-Tapia, J.C. Díaz-Rosado, A. Alvarez-Risco, S. Del-Aguila-Arcentales, N.M. Davies, J.A. Yáñez, C. Vera-Gonzales, Optimization of Synthesis of Silver Nanoparticles Conjugated with Lepechinia meyenii (Salvia) Using Plackett-Burman Design and Response Surface Methodology—Preliminary Antibacterial Activity, Processes. 10 (2022) 1727. https://doi.org/10.3390/pr10091727.

[33] A. Mohammadpour, N. Karami, R. Zabihi, E. Fazeliyan, A. Abbasi, S. Karimi, M. de Farias, M.G. Adeodato Vieira, E. Shahsavani, A. Mousavi Khaneghah, Green synthesis, characterization, and application of Fe3O4 nanoparticles for methylene blue removal: RSM optimization, kinetic, isothermal studies, and molecular simulation, Environ Res. 225 (2023) 115507. https://doi.org/10.1016/j.envres.2023.115507.

[34] I. Ben Amor, H. Hemmami, S.E. Laouini, M.S. Mahboub, A. Barhoum, Sol-Gel Synthesis of ZnO Nanoparticles Using Different Chitosan Sources: Effects on Antibacterial Activity and Photocatalytic Degradation of AZO Dye, Catalysts. 12 (2022) 1611. https://doi.org/10.3390/catal12121611.

[35] A. Turcu Stiolica, M. Popescu, M.V. Bubulica, C.N. Oancea, C. Nicolicescu, C.V. Manda, J. Neamtu, O. Croitoru, Optimization of Gold Nanoparticles Synthesis using Design of Experiments Technique, Revista de Chimie. 68 (2017) 1423–1518. https://doi.org/10.37358/rc.17.7.5707.

[36] F. Mérida, Optimization of synthesis and peptization steps to obtain iron oxide nanoparticles with high energy dissipation rates, J Magn Magn Mater. 394 (2015) 361–371. https://doi.org/10.1016%2Fj.jmmm.2015.06.076.

[37] C. Chou, S. Chen, Phase equilibria of the Sn–Zn–Cu ternary system, Acta Mater. 54 (2006) 2393–2400. https://doi.org/10.1016/j.actamat.2006.01.014.

[38] F. Jing, Y. Liu, Y. Du, C. Shi, B. Hu, X. He, Phase Equilibria, Thermodynamics and Solidified Microstructure in the Copper–Zirconium–Yttrium System, Materials. 16 (2023) 2063. https://doi.org/10.3390/ma16052063.

[39] O.D. Neikov, Mechanical Alloying, Handbook of Non-Ferrous Metal Powders. (2009) 63–79. https://doi.org/10.1016/b978-1-85617-422-0.00003-3.

[40] X. Cheng, Z. Wang, K. Nakamoto, K. Yamazaki, A study on the micro tooling for micro/nano milling, The International Journal of Advanced Manufacturing Technology. 53 (2011) 523–533. https://doi.org/10.1007/s00170-010-2856-3.

[41] L.P. Arendsen, R. Thakar, A.H. Sultan, The Use of Copper as an Antimicrobial Agent in Health Care, Including Obstetrics and Gynecology, Clin Microbiol Rev. 32 (2019). https://doi.org/10.1128/cmr.00125-18.

[42] T.J. Silhavy, D. Kahne, S. Walker, The Bacterial Cell Envelope, Cold Spring Harb Perspect Biol. 2 (2010) a000414–a000414. https://doi.org/10.1101/cshperspect.a000414.